

MASH: Masked Anchored SpHirical Distances for 3D Shape Representation and Generation

CHANGHAO LI, University of Science and Technology of China, China

YU XIN, University of Science and Technology of China, China

XIAOWEI ZHOU, State Key Laboratory of CAD & CG, Zhejiang University, China

ARIEL SHAMIR, Reichman University, Israel

HAO ZHANG, Simon Fraser University, Canada

LIGANG LIU, University of Science and Technology of China, China

RUIZHEN HU, Shenzhen University, China

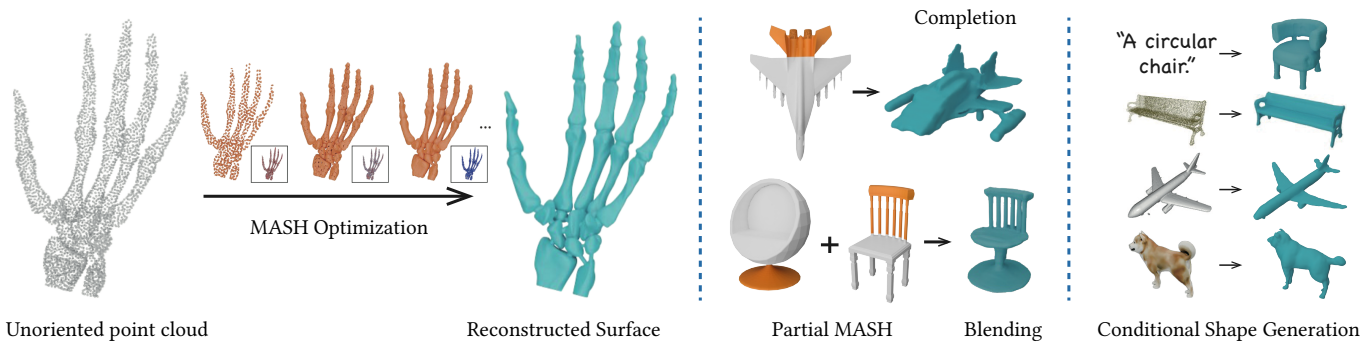


Fig. 1. MASH represents a 3D shape by fitting a set of *Masked Anchored SpHirical distance functions* as observed from the perspective of a fixed number of anchor points in 3D space. Left shows an iterative optimization of MASH parameters, from an unoriented point cloud, leading to closer and closer approximations to the ground-truth shape surface. Middle and right show the versatility of MASH in enabling a variety of downstream applications including shape completion, blending, and conditional 3D generation from multi-modal inputs including text prompts, point clouds, and single-view images. On the right: top three results were obtained by training the generator on ShapeNet, while the bottom (the dog) result was obtained on training with Objaverse.

We introduce *Masked Anchored SpHirical Distances (MASH)*, a novel *multi-view* and *parametrized* representation of 3D shapes. Inspired by multi-view geometry and motivated by the importance of perceptual shape understanding for learning 3D shapes, MASH represents a 3D shape as a collection of *observable local surface patches*, each defined by a spherical distance function emanating from an anchor point. We further leverage the compactness of spherical harmonics to encode the MASH functions, combined with a *generalized view cone* with a parameterized base that *masks* the spatial extent of the spherical function to attain locality. We develop a differentiable optimization algorithm capable of converting any point cloud into a MASH representation

accurately approximating ground-truth surfaces with arbitrary geometry and topology. Extensive experiments demonstrate that MASH is versatile for multiple applications including surface reconstruction, shape generation, completion, and blending, achieving superior performance thanks to its unique representation encompassing both implicit and explicit features.

CCS Concepts: • Computing methodologies → Shape modeling; Neural networks.

ACM Reference Format:

Changhao Li, Yu Xin, Xiaowei Zhou, Ariel Shamir, Hao Zhang, Ligang Liu, and Ruizhen Hu. 2025. MASH: Masked Anchored SpHirical Distances for 3D Shape Representation and Generation. *ACM Trans. Graph.* 1, 1 (April 2025), 11 pages. <https://doi.org/10.1145/nnnnnnn.nnnnnnn>

1 INTRODUCTION

In a recent position paper by Ramamoorthi on NeRFs [2023], the importance of finding the *right 3D representation* was highlighted in that the success of NeRFs is not due to a particular learning representation or algorithm, but rather in the idea of using a continuous volumetric representation. In the same manner, the success of 3D Gaussian splatting [Kerbl et al. 2023] may be seen as yet another win for choosing a better representation, this time point primitives, for novel view synthesis. Still, to date, despite a plethora of representations for 3D shapes that have emerged in computer graphics,

Authors' addresses: Changhao Li, University of Science and Technology of China, Hefei, China, lch0510@mail.ustc.edu.cn; Yu Xin, University of Science and Technology of China, Hefei, China, xy0731@mail.ustc.edu.cn; Xiaowei Zhou, State Key Laboratory of CAD & CG, Zhejiang University, Hangzhou, China, xwzhou@zju.edu.cn; Ariel Shamir, Reichman University, Herzliya, Israel, arik@ruri.ac.il; Hao Zhang, Simon Fraser University, Vancouver, Canada, haoz@cs.sfu.ca; Ligang Liu, University of Science and Technology of China, Hefei, China, lgliu@ustc.edu.cn; Ruizhen Hu, Shenzhen University, Shenzhen, China, ruizhen.hu@gmail.com.

Permission to make digital or hard copies of all or part of this work for personal or classroom use is granted without fee provided that copies are not made or distributed for profit or commercial advantage and that copies bear this notice and the full citation on the first page. Copyrights for components of this work owned by others than ACM must be honored. Abstracting with credit is permitted. To copy otherwise, or republish, to post on servers or to redistribute to lists, requires prior specific permission and/or a fee. Request permissions from permissions@acm.org.

© 2025 Association for Computing Machinery.
0730-0301/2025/4-ART \$15.00
<https://doi.org/10.1145/nnnnnnn.nnnnnnn>

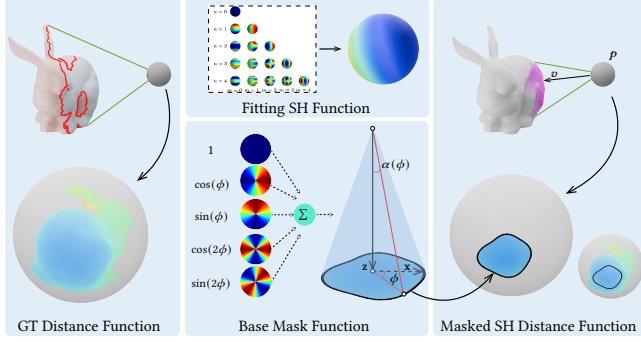


Fig. 2. Parametric representation of MASH for a single anchor.

there is no universal agreement as to what the “best” 3D shape representation is. This is the motivation of our current work.

We begin with Signed Distance Fields (SDFs), inspired by their recent success, which has propelled the advancement of neural fields [Xie et al. 2022]. An SDF stores a *single* scalar which reflects the closest distance to a surface. Although simple and fundamental, it is neither the most informative nor the most efficient since many samples have to be taken to closely define a surface.

From the perspective of multi-view geometry and treating each point in space as a viewpoint, a large amount of surface information can be *observed*. As we scale up per-point information, we can reduce the number of points (views) needed to capture the underlying surface, striving for a better tradeoff between representational capacity and compactness. Taking such a *perceptual* approach to represent 3D shapes accentuates shape *understanding*. This is critical to any learning task that relies on such an understanding to compensate for the ill-posed nature of the task due to sparse inputs. Primary examples of such tasks include single-view 3D reconstruction, shape completion, and text-to-3D generation.

In this work, we introduce a novel *multi-view* and *parametric* representation of 3D shapes called *Masked Anchored SpHerial (MASH)* distances. Inspired by multi-view geometry, MASH represents a 3D shape as a collection of *observable local surface patches*, each defined by a spherical distance function emanating from an anchor point of observation. However, the creation of such a representation is not straightforward. Key questions include how to parametrize the spherical distance functions and the precise demarcation of their view ranges. Achieving a balance is paramount, that is, we aim to minimize the overlap between the local regions associated with different anchors while ensuring that the local connectivity between adjacent patches remains intact. To address this, MASH leverages the mathematical elegance of *spherical harmonics*, combined with a *generalized view cone* with a parameterized base that *masks* the spatial extent of the spherical function; see Figure 2. This leads to a compact and smooth representation of local surfaces.

Our new 3D shape representation presents several distinct features. First, each spherical function in MASH is significantly more informative than a single closest distance as in an SDF, while the need for much fewer spherical functions (about 400) and the use of spherical harmonics enable a compact representation that maintains local surface smoothness and continuity. Second, the masking

technique ensures that each patch can be accurately approximated by spherical harmonics and provides a balance among patches to avoid computational redundancy. To further ensure efficient optimization and adaptation to the geometric details of a shape, we introduce a differentiable optimization scheme for MASH based on its parameterized representation, which consists of several novel key components including differentiable point sampling, anchored inverse transformation, and a two-step optimization strategy with tailored loss functions; these are explained in detail in Section 3.2.

As a compact, parametrized, and patch-based representation, MASH offers several unique advantages in downstream applications and its versatility is at display in Figure 1. To start, MASH is inherently equipped to handle complex topologies and can be iteratively refined to closely approximate 3D shapes from even un-oriented point clouds. Additionally, being parameterized, MASH provides a natural embedding for 3D shapes and thus can be used for shape generation, with the generative model producing MASH representations directly instead of some intermediate, typically non-interpretable, implicit features. The compactness introduced by the MASH parametrization as well as the fact that different shapes can share similar *local* surface patches makes our MASH-based generative models easier to train and converge faster than alternative representations. Moreover, being patch-based hence with local support, MASH further allows explicit editing of the generated shapes, which is difficult to achieve with purely implicit representations. More specifically, any subset of the anchors and thus its associated surface patches can be frozen during shape generation to facilitate applications such as shape completion or blending.

Our extensive experiments validate the effectiveness of MASH in reconstructive and generative tasks over traditional and implicit representations. Our main technical contributions include:

- MASH, a novel multi-view and parametrized representation for 3D shapes that accurately captures the surfaces of objects with arbitrary geometry and topology.
- A differentiable MASH optimization capable of converting any input point cloud into a precise MASH representation.
- MASH is versatile for multiple applications including surface reconstruction, shape generation, completion, and blending, achieving superior performance thanks to its unique representation encompassing both implicit and explicit features.

2 RELATED WORK

3D Shape Representations. Point clouds, meshes, and voxel grids are the most commonly used explicit 3D representations. Point cloud is a sparse, high-resolution representation, but its unordered nature makes it difficult to process. Triangle meshes deliver more detailed surface geometry than point clouds and are favored for tasks that require more accurate surface representation [Gong et al. 2019; Hanocka et al. 2019; Lim et al. 2018], but the complex topology makes meshes hard to encode and generate. Voxel grids, as a natural extension from 2D pixels, are easier to process thanks to their rasterized nature and are thus widely used for shape reconstruction and generation [Brock et al. 2016; Choy et al. 2016; Dai et al. 2017; Girdhar et al. 2016; Wu et al. 2016, 2015]. However, their memory consumption grows exponentially as the resolution increases.

Implicit representations [Calakli and Taubin 2012; Hoppe et al. 1992; Kazhdan et al. 2006; Kazhdan and Hoppe 2013; Lin et al. 2022], including those based on neural networks, have become increasingly popular. They encode shapes within continuous functions like signed distance functions [Calakli and Taubin 2012; Park et al. 2019] or occupancy fields [Mescheder et al. 2019; Peng et al. 2020], offering flexibility and the ability to represent complex topologies smoothly. However, the implicit nature of these representations forbids explicit shape editing. Parametric methods like spline surfaces [Gordon and Riesenfeld 1974; Iglesias et al. 2004] and spherical harmonics [Saupe and Vranić 2001] achieve compact representations but lack accurate methods for estimating parametric representations for shapes.

Our MASH representation combines the advantages of those representations, with the set of anchors resembling the flexibility of the point clouds, the surface patches parametrized with each anchor providing more detailed geometry, and the parametrization itself providing a natural implicit embedding for 3D shapes.

Surface Reconstruction. Early methods reconstruct surfaces from point clouds using Voronoi/Delaunay structures [Amenta et al. 1998, 2001; Dey and Goswami 2004], α -shapes [Edelsbrunner and Mücke 1994], or ball pivoting [Bernardini et al. 1999], but struggle with nonuniform or noisy data. Thus learning-based approaches are used to improve the accuracy of connectivity prediction [Rakotosaona et al. 2021]. Since the iso-surface can be extracted by Marching Cubes [Lorensen and Cline 1987], some works start to focus on seeking an implicit function [Kazhdan et al. 2006; Kazhdan and Hoppe 2013; Wang et al. 2023], while others try to enhance normal consistency [Hoppe et al. 1992; Lin et al. 2022; Metzer et al. 2021].

Among prior works, ARO-Net [2023] is most related as it also utilizes partial observations at a set of anchors for surface reconstruction. However, their observation is oriented to a query point for occupancy prediction and there is no parameterization or optimization involved. Unlike all these works, we obtain an explicit parametric representation by optimizing MASH directly from a point cloud, and then extract the surface from the MASH.

3D Shape Generation. Recent advances in 2D image generation, such as DALL-E [Ramesh et al. 2021], Imagen [Saharia et al. 2022], and Stable Diffusion [Rombach et al. 2022], have inspired 3D generation methods that leverage 2D priors. DreamFusion [Poole et al. 2022] introduces Score Distillation Sampling (SDS) to optimize 3D shapes via NeRF [Mildenhall et al. 2021], and some works focus on extending the concept of SDS to various neural domains [Li et al. 2023; Liu et al. 2023]. However, these methods suffer from a long optimization time and inconsistent multi-view outputs. Another line of work for 3D shape generation is to directly train and generate 3D representations. Early methods [Choy et al. 2016; Mescheder et al. 2019] primarily utilize 3D convolutional networks to encode and decode 3D voxel grids. Point-E [Nichol et al. 2022] innovatively employs a diffusion model based on the pure transformer network structure to directly generate point clouds. Polygen [Nash et al. 2020] and MeshGPT [Siddiqui et al. 2024] proposed to generate meshes by serializing the vertices and faces of a mesh, generating high-quality results, but their reliance on high-quality datasets limits their generality. Later, with the advent of Variational Autoencoder (VAE), many works [Cheng et al. 2023; Gupta et al. 2023; Jun and

Nichol 2023; Zhang et al. 2023; Zhao et al. 2024] use VAE to encode 3D shapes and decode them into occupancy or distance fields, and generate shapes in the encoded latent space. Unlike those methods, we adopt the explicit parametrized MASH representation directly for generation, improving efficiency while maintaining accuracy.

3 METHOD

In this section, we first explain the parametric representation of MASH in Section 3.1, and then show how to optimize the MASH representation for a given shape in Section 3.2.

3.1 MASH Representation

Given a 3D shape S and a point p in space, we can define the visible region on the surface of S from the perspective of p by casting rays from p in all directions, forming a spherical distance function centered at the anchor point p , as shown in Figure 2 (left). Such visible regions have been studied for shape partition [Shapira et al. 2008], reconstruction [Shalom et al. 2010], and relationship optimization between two shapes [Zhao et al. 2016], all suggesting that visible regions can accurately characterize local shape features, while global structures of a 3D shape can be faithfully captured from a set of anchor points all around the surface of the shape.

Our goal is to define a parameterized representation of these visible regions such that a 3D shape can be represented by a set of anchored parameters, with a simple and compact structure. To this end, it is natural to consider using a set of spherical harmonics to approximate the visible region represented by a spherical distance function. However, the spherical distance function is discontinuous when shifting from one surface region to other unconnected regions, as well as when crossing view boundaries. Such discontinuities hinder the use of spherical harmonics for an accurate approximation of an entire distance function. The key idea of MASH is to further introduce a *mask* to constrain the approximation region so that even low-order spherical harmonics can provide a faithful approximation. Specifically, the mask is defined by a generalized 3D view cone with a parameterized free-form base.

Therefore, each anchor of our MASH can be represented by a set of parameters $\mathcal{A} = \{p, v, C, \mathcal{V}\}$, where p is the location of the anchor, v refers to the view direction, C and \mathcal{V} are two subsets of parameters used to define the corresponding spherical distances and vision mask. Figure 2 shows our MASH representation for a single anchor point. The two subsets of parameters C and \mathcal{V} are visualized in the middle, and the continuous visible region characterized by our MASH representation is shown on the right.

Parameterized spherical distances. We use a combination of spherical harmonics to represent the spherical distance function as follows:

$$d_C(\theta, \phi) = \sum_{l=0}^{L=L} \sum_{m=-l}^{m=l} C_l^m Y_l^m(\theta, \phi), \quad (1)$$

where Y_l^m is the spherical harmonics at frequency l and C_l^m are the corresponding combination coefficients. Thus, the SH parameters are defined as

$$C = \{C_l^m | |m| \leq l, l = 0, 1, \dots, L\}. \quad (2)$$

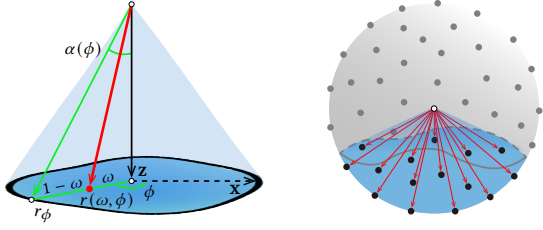


Fig. 3. Differentiable MASH point sampling. Parametrization of any ray sampled inside the view cone (left) and pre-sampled rays filtered by the view cone (right), with each ray corresponding to one sample point.

Parameterized vision mask. We use a generalized 3D view cone to constrain the vision field and define the mask on the sphere. Note that the common right circular cone with a fixed angle α can only define a circular region on the sphere, which cannot characterize the free-form surface boundary obtained when viewing from a certain direction as shown in Figure 2 (left). Therefore, we generalize the 3D view cone with an anisotropic vision angle $\alpha(\phi)$, where $\phi \in [0, 2\pi]$ defines a circle around the Z-axis direction and $\alpha(\phi)$ is the maximal view range corresponding to each ϕ , as shown in Figure 2 (middle).

Note that $\alpha(\phi)$ is a periodic function, thus it can also be approximated by trigonometric interpolation as follows:

$$\alpha(\phi) = 2\pi\sigma(a_0 + \sum_{k=1}^K a_k \cos(k\phi) + \sum_{k=1}^K b_k \sin(k\phi)), \quad (3)$$

where

$$\sigma(x) = \frac{1}{1 + e^{-x}}. \quad (4)$$

Thus, the vision mask can be defined by the set of parameters:

$$\mathcal{V} = \{a_0, a_1, b_1, \dots, a_K, b_K\}. \quad (5)$$

3.2 MASH Optimization

Given a 3D shape S , either represented by a mesh or a point cloud, our goal of MASH optimization is to find a set of anchors with associated parameters $\{\mathcal{A}_i\}_{i=1}^M = \{p_i, v_i, C_i, \mathcal{V}_i\}_{i=1}^M$ that have a high approximation quality.

To enable differentiable optimization of $\{\mathcal{A}_i\}$, we first define a differential operator to sample points from the surface patches defined by our MASH representations, and then use chamfer distance between those points to the points from the given shape to measure the approximation error and guide the optimization.

Moreover, note that for each anchor, intuitively, \mathcal{V} defines a local patch on a sphere, and C characterizes the local geometry of such surface patch, as shown in Figure 2 (right). As C is a set of SH parameters, it can be used to represent a spherical surface more precisely than a planar surface. To further boost the representability of the spherical harmonics, we also introduce the inverse transformation [Katz and Tal 2015] that can convert planar surfaces of the given shape into spherical surfaces and thus make them easier to fit.

Differentiable point sampling. To sample points on the surface patches defined by each anchor is essentially to sample rays inside the corresponding 3D vision cones, as each ray will intersect with

the surface patch at one unique point. Moreover, each ray will also intersect with the base mask at one unique point and thus be represented by two parameters $\{\omega, \phi\}$ inside the base mask as shown in Figure 3 (left).

More specifically, $\phi \in [0, 2\pi]$ defines a point on the mask boundary, and $\omega \in [0, 1]$ determines the interior point on the line segment connecting the boundary point and the center, and the ray shooting from the anchor to that interior point be calculated by the spherical linear interpolation [Pennec 1998]:

$$r(\omega, \phi) = \text{slerp}(\mathbf{z}, r_\phi, \omega), \quad (6)$$

where \mathbf{z} is the Z-axis direction and r_ϕ is the ray shooting from the anchor to the boundary point determined by ϕ :

$$r_\phi = (\sin(\alpha(\phi)) \cos \phi, \sin(\alpha(\phi)) \sin \phi, \cos(\alpha(\phi))), \quad (7)$$

with $\alpha(\phi)$ defined by Equ. (3).

Now with the sampled ray $r(\omega, \phi)$, the corresponding intersecting point on the surface patch can be obtained by moving the anchor along the ray with the corresponding spherical distance $d(\alpha(\phi), \phi)$ defined by Equ. (1). As all the computation so far is conducted in the local coordinate of the anchor, to get the final position of the points on the surface, we still need to apply transformation determined by the position p and view direction v of the anchor. Therefore, the final surface point can be obtained as follows:

$$\hat{p}(\omega, \phi) = p + \mathbf{R}_v \cdot d(\omega\alpha(\phi), \phi) \cdot r(\omega, \phi), \quad (8)$$

where \mathbf{R}_v is the rotation matrix determined by v and defined as:

$$\mathbf{R}_v = \cos \theta_v \mathbf{I} + (1 - \cos \theta_v) \mathbf{k} \mathbf{k}^T + \sin \theta_v \mathbf{k} \mathbf{K}, \quad (9)$$

with

$$\mathbf{k} = \frac{\mathbf{v}}{\|\mathbf{v}\|}, \quad \theta_v = \|\mathbf{v}\|, \quad \mathbf{K} = \begin{bmatrix} 0 & -k_z & k_y \\ k_z & 0 & -k_x \\ -k_y & k_x & 0 \end{bmatrix}. \quad (10)$$

Note that to uniquely determine \mathbf{R}_v from v as above, v does not directly record the exact view direction of the anchor, but instead stores the rotation axis (in direction k) and rotation angle (in magnitude θ_v), which are used to rotate the local coordinate of the anchor so that the Z-axis is pointing to the view direction.

To sample a set of rays inside the view cone, one straightforward way is to uniformly sample $\omega \in [0, 1]$ and $\phi \in [0, 2\pi]$. However, this kind of sampling usually leads to non-uniform distribution of corresponding sample points on the surface patch, with local regions staying farther to the anchor get sparse points. To ensure more uniform sampling on the surface patches, we pre-sample uniform points on a unit sphere and then select the subset of points inside our view cone for the shooting rays, as shown in Figure 3 (right).

In more detail, we first uniformly sample N_{dir} points on the unit sphere using Fibonacci sampling [Keinert et al. 2015]. Therefore, we have a set of pre-defined ray directions parametrized in the spherical coordinate $\{\theta_j^{\text{pre}}, \phi_j^{\text{pre}}\}$, with

$$\theta_j^{\text{pre}} = \arccos(1 - \frac{2 \cdot j - 1}{N_{\text{dir}}}), \quad j \in [1, N_{\text{dir}}], \quad (11)$$

$$\phi_j^{\text{pre}} = (1 + \sqrt{5}) \cdot \pi \cdot (j - 0.5), \quad j \in [1, N_{\text{dir}}]. \quad (12)$$

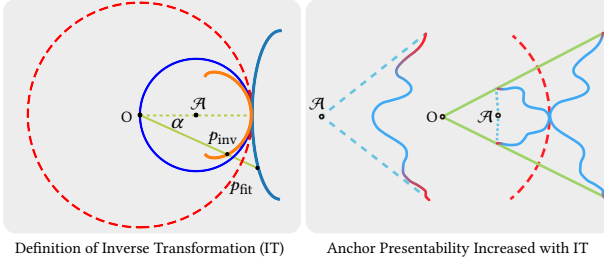


Fig. 4. Anchored inverse transformation.

Then, we can convert those two parameters into the local coordinate of our base mask $\{\omega_j^{\text{pre}}, \phi_j^{\text{pre}}\}$ with $\omega_j^{\text{pre}} = \theta_j^{\text{pre}} / \alpha(\phi_j^{\text{pre}})$, and then filter the parametric pre-sampled directions with $\omega_j^{\text{pre}} \in [0, 1]$.

Anchored inverse transformation. The goal of applying inverse transformation is to enlarge the visible region of each anchor when given the fixed degree of spherical harmonics and approximation threshold, such that we can use fewer anchors to reach to the same level of approximation.

Figure 4 illustrates the definition of inverse transformation (left) and how the anchor is able to approximate the given surface after applying the inverse transformation (right). The curve shown on the right represents the surface that needs to be approximated with MASH, and the colormap on top of it indicates the fitting error, with red corresponding to a larger error. After inverse transformation, this surface is bent around the anchor, making it easier for spherical harmonics to fit and leading to lower fitting error, which results in a larger fitting region to the anchor.

For a more formal definition of the inverse transformation, we first define the center of the inverse transformation O , within the local coordinate of each anchor, as:

$$O = -h \cdot \mathbf{z} \quad (13)$$

where h is the distance from the anchor along \mathbf{z} to its parametric surface, which can be approximated by the first SH parameter C_0^0 for fast computation. Next, we introduce the transformations between the target fitting point p_{fit} on the source surface and target inverse point p_{inv} :

$$p_{\text{inv}} = O + \frac{R^2}{\|p_{\text{fit}} - O\|^2} \cdot (p_{\text{fit}} - O), \quad (14)$$

$$p_{\text{fit}} = O + \frac{R^2}{\|p_{\text{inv}} - O\|^2} \cdot (p_{\text{inv}} - O). \quad (15)$$

where $R = 2C_0^0$ is the radius of the inverse sphere. We apply the inverse transformation to the parametric points sampled on the patch surfaces using Equ. (15) before rotating and translating them.

Loss function. Given the points Q sampled on the source shape and the parametric points P sampled on the MASH patches, we now define the losses that are used to guide the optimization of our MASH parameters. First, we utilize the L1 Chamfer Distance and split the two main terms as the fitting loss term L_f and coverage

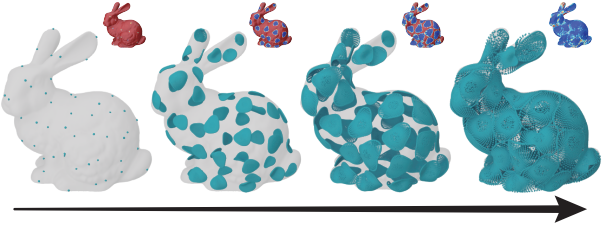


Fig. 5. MASH optimization process.

loss term L_c individually:

$$L_f(P, Q) = \frac{1}{|P|} \sum_{p \in P} d(p, Q), \quad (16)$$

$$L_c(P, Q) = \frac{1}{|Q|} \sum_{q \in Q} d(q, P), \quad (17)$$

where the point-to-set distance is defined as $d(p, Q) = \min_{q \in Q} \|p - q\|_2$.

Note that L_f will make the sampled points P to be closer to the input point cloud Q , while L_c will make the sampled points P cover as more points in Q as possible. Thus, we can control the moving trend of P by setting different weights for these two loss items.

However, these loss terms only measure the distances between discrete point sets, which encourage anchors to cover the input point cloud, neglecting the continuity between surfaces corresponding to adjacent anchors. Therefore, we propose a new boundary-continuous loss function to improve the connectivity of anchor mask boundaries, which is defined as:

$$L_b(P) = \frac{1}{M} \sum_{i \in [1, M]} \frac{1}{|P_i|} \sum_{p \in P_i} d(p, \bigcup_{j \neq i} P_j), \quad (18)$$

where M is the number of anchors, P_i is the sampled points located on the mask boundary of i -th anchor. Our complete loss function is then defined as:

$$L = \omega_f L_f + \omega_c L_c + \omega_b L_b. \quad (19)$$

Note that all the equations we defined so far have analytical expressions, and thus we can calculate the derivatives of all MASH parameters with respect to the final loss value through the composition of these functions using the chain rule for differentiation. Therefore, our whole optimization scheme is differentiable.

Optimization process. We adopt a two-step optimization strategy that first makes sure the full coverage of the source shape and then refines the local details. The optimization process for the bunny with $M = 50$ anchors is illustrated in Figure 5, with the fitting error on each step shown on the top right corner.

For initialization, we first uniformly sample M points from the source point cloud Q , and then move those points along their locally estimated normal direction with a pre-defined small distance d_{init} to get the initial locations of all the anchors, with each anchor pointing to the corresponding sampled point. All the remaining parameters are set to 0, except $C_0^0 = d_{\text{init}}/Y_0^0$, to initialize the surface patch corresponding to each anchor as a planar disk close to the source shape after inverse transformation.

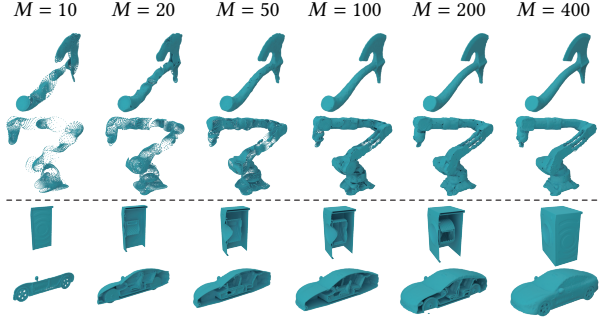


Fig. 6. MASH optimization results with different anchor numbers (top) and for shapes with inner or thin structures (bottom).

Note that the boundary-continuous loss L_b defined in Equ. (18) is mainly used to improve the boundary continuity between anchor patches, so it is only introduced when the main task of approximating the source shape is completed. Therefore, in the first stage of the optimization, we set $\omega_b = 0$ to ensure that anchors can expand along and cover the source shape, with $\omega_f = 1$ and ω_c linearly increasing from 0.5 to 1. Once 80% of the source shape is covered, we enter the second stage of the optimization by linearly increasing ω_b from 0 to 1, to ensure that each anchor continues to prioritize fitting the object surface as its main objective and at the same time enhance the connectivity between adjacent anchors. The optimization continues until the loss L defined in Equ. (19) converges.

4 EXPERIMENTS AND RESULTS

In this section, we first show the expressive power of the proposed MASH representation in Section 4.1, and then demonstrate how MASH can be used in two different applications, including surface reconstruction in Section 4.2 and shape generation in Section 4.3.

4.1 Shape Approximation

The key hyperparameters in our MASH representation are anchor numbers M , mask degrees K , and spherical harmonic degrees L , and the total number of MASH parameters N can be calculated as $N = M(2K+1+(L+1)^2+6)$. The representation ability of MASH will grow with the increase of M , K , and L . However, a larger number of parameters will lead to a reduction in computational efficiency. In all our experiments, we set $M = 400$, $K = 3$, and $L = 2$. Under this setting, it takes an average of about 39 seconds to fit a single object and the calculation of the loss terms takes approximately 80% of the total time. More quantitative comparisons of the results with different hyperparameters and the effect of applying inverse transformation can be found in the supplementary material.

Figure 6 (top) shows some MASH optimization results with different anchor numbers, with the surface patch represented by each anchor visualized using a set of sampled points. We can see that even with only 10 anchors, MASH can faithfully capture shape with a set of bent patches. With the increase of anchor number M , the approximate error becomes smaller, and the sharp features are better preserved. Note that there is no assumption on the topology of the

Table 1. Quantitative comparison with surface reconstruction baselines on the ShapeNet-V2 dataset. For ease of comparison of results, we multiply the L1 Chamfer Distance by 1000 here.

Method	SPR+PCA	PGR	ConvONet	ARONet	MASH-Mesh	MASH	FPS
L1-CD↓	89.565	6.381	17.732	15.697	5.450	4.944	4.782
L2-CD↓	429.112	26.876	72.523	66.051	22.523	2.268	1.871
FScore↑	0.497	0.988	0.812	0.880	0.997	0.998	0.999
$D_H \downarrow$	0.272	0.023	0.131	0.117	0.019	0.013	0.012
$S_{cos} \uparrow$	0.684	0.974	0.821	0.898	0.980	0.984	0.991
NIC↓	65.023	19.178	29.810	23.035	18.040	13.346	6.230

Table 2. Quantitative comparison of category-conditioned generation with different methods.

	R-KID ↓	R-FID ↓	P-KID ↓	P-FID ↓
LN3Diff	0.222	247.379	0.792	150.578
3DShape2VecSet	0.138	173.649	0.146	38.021
Ours	0.136	163.473	0.093	30.344

given shape, and MASH can be used to approximate shapes with inner or thin structures as shown in Figure 6 (bottom).

4.2 Surface Reconstruction

MASH surface extraction. For a given point cloud, we can optimize our MASH representation as described in Section 3.2. To further extract a watertight surface, we first estimate the normals on points P sampled on our surface patches and then extract the iso-surface with marching cubes on octrees with a maximum depth 10, similar to the Poisson reconstruction algorithm [Kazhdan and Hoppe 2013].

Note that each patch in MASH already provides a consistent normal orientation for the points inside, we only need to find a globally consistent orientation for all the patches. More specifically, for the k -th sampled point of i -th anchor p_k^i in the sampled points P , we first obtain its normal n_{src} , with more details provided in the supplementary material. Then we sample a subset of points P' from P by furthest point sampling and estimate their normals using PGR [Lin et al. 2022]. Once the globally consistent normals for the point set P' are obtained, we reverse the normal direction of patches where the orientation is inconsistent with those points in P' , and then perform a smooth normal interpolation for better continuity between boundaries, defined as:

$$n_k^i = \text{slerp}(n_{src}, n_{pgr}, \sqrt{\omega_k^i}), \quad (20)$$

where n_{pgr} is the normal of the nearest point $p' \in P'$ of p_k^i , and $\omega_k^i \in [0, 1]$ is the corresponding mask parameter indicating how p_k^i is close to the center of the belonging patch.

Comparison to baselines. We compare our method to Screened Poisson Reconstruction (SPR) [Kazhdan and Hoppe 2013] and several other representative reconstruction methods, including Parametric Gauss Reconstruction (PGR) [Lin et al. 2022], Convolutional Occupancy Networks (ConvONet) [Peng et al. 2020], and ARONet [Wang et al. 2023]. PGR is the SOTA learning-free surface reconstruction method from point clouds without normals, while ConvONet and ARONet are both learning-based methods. We conduct experiments on the full dataset of ShapeNet-V2 [Chang et al. 2015].

Table 3. Quantitative comparison of image-conditioned generation with different methods.

	CD ↓	EMD ↓	F-Score ↑	R-KID ↓	R-FID ↓	P-KID ↓	P-FID ↓	ULIP-I ↑
InstantMesh	23.112	4.162	0.840	0.056	179.755	0.079	74.720	5.552
Make-a-Shape	31.105	4.192	0.664	0.032	161.428	0.074	49.857	7.360
Hunyuan3D-1	11.227	3.166	0.879	0.023	160.322	0.036	51.534	6.367
Ours	9.555	2.151	0.837	0.018	156.141	0.005	25.074	7.530

From the comparison results in Table 1, we can see that our method performs better than all baselines. As shown in Figure 8, our MASH representation has a stronger ability to describe the surface of 3D shapes and can reconstruct a smoother and more accurate surface which conforms to the spatial distribution of the given point cloud. Especially for more challenging objects with thin planes or dense grid structures, most methods tend to ignore these geometric features, resulting in insufficient reconstruction or blending multiple surfaces together, while our method can more accurately distinguish point sets with adjacent relationships in the point cloud. Our method is also more robust to noisy inputs, and we show some representative results with different noise levels in Figure 9. More details about the experiment setup, evaluation metrics, results for per-category comparison, and explanations about the experiments on noisy point clouds are provided in the supplementary materials.

4.3 Shape Generation

As a compact parametric representation, MASH provides a natural embedding for 3D shapes. We show how MASH can be further used for shape generation in two most common settings, i.e., category-conditioned and image-conditioned. For both settings, we chose the same network backbone as in 3DShape2VecSet [Zhang et al. 2023], as MASH consists of an unordered set of anchor parameters. Then, for the category-conditioned model, we create a learnable embedding vector for each category and inject it as a condition into the network. For the image-conditioned model, we extract the image features using the pre-trained DINOv2-ViT-B/14 model [Oquab et al. 2023]. More details are provided in the supplementary material.

Category-conditioned generation. We train the category-conditioned model on the ShapeNet-V2 dataset [Chang et al. 2015] and compare our method with LN3Diff [Lan et al. 2025] and 3DShape2VecSet (S2V) [Zhang et al. 2023]. Thanks to the compactness of MASH, the training of our network converges much quicker than other methods. Compared to S2V, both the training and sampling time of our model is less than one-third, with the same network backbone.

To measure the mesh quality of the generative model, we follow CLAY [Zhang et al. 2024] to use Render-FID, Render-KID, P-FID, and P-KID as metrics, computed on 200 generated shapes and shapes random selected from the ShapeNet-V2 dataset for each category. Quantitative and qualitative comparisons are presented in Table 2 and Figure 10, respectively. From the comparisons, we can see that the shapes generated based on MASH exhibit a high diversity and have nice geometric details.

Moreover, as an explicit patch-based representation, one unique feature of MASH is that a subset of its anchors can be fixed during the generation, which enables novel applications like part-conditional

generation and shape blending. More specifically, during the training of our category-conditioned model, we replace a random proportion of the initial noise fed into the generative model with the parameters of the ground truth MASH in 80% of the steps. With this modification, our trained category-conditioned generative model can naturally support completion and blending tasks. Some visual examples are shown in Figure 7. We can see that the generative model fully utilizes the information of the fixed anchors and attempts to provide reasonable completion or blending results, with all fixed parts are nicely preserved. Note that the slight change of local geometry of the given part is mainly due to surface extraction.

Image-conditioned generation. We train the image-conditioned model on the Objaverse-82K dataset [Deitke et al. 2023] and compare our method to baselines including InstantMesh [Xu et al. 2024], Make-A-Shape [Hui et al. 2024] and Hunyuan3D-1 [Yang et al. 2024]. To perform a quantitative comparison, we randomly select 100 3D shapes from the Objaverse dataset and render an image from a random viewpoint for each shape to serve as the input of different methods. Then, we normalize the 3D shapes generated by different methods together with the 3D shapes in the dataset and manually align them to eliminate any possible orientation inconsistencies between the generated results and the ground truth. Other than the metrics used for category-conditioned generations, we also introduce Chamfer Distance (CD), Earth Mover’s Distance (EMD), F-Score, and ULIP-I as additional metrics. The quantitative and qualitative comparisons are shown in Table 3 and Figure 11, respectively. Our method obtains generally better results. Both InstantMesh and Hunyuan3D-1 take the input image to generate multi-view images first and then reconstruct the 3D shape from those images, thus they highly depend on the geometric consistency across multiple views. Compared to other methods, the 3D shapes generated based on MASH can better preserve the topology of the object in the image and better recover the full geometric shape.

5 CONCLUSION

We introduce a new *multi-view* and *parametrized* 3D shape representation, coined Masked Anchored SpHercical Distances (MASH), to efficiently and accurately parameterize a given 3D shape. With a differentiable MASH optimization algorithm, we can convert discrete data structures such as point clouds into continuous surface-based representations efficiently. Moreover, we demonstrate that MASH is quite versatile for various applications including surface reconstruction, shape completion, blending, and generations. Extensive experiments and comparisons are conducted to validate the effectiveness of our new representation.

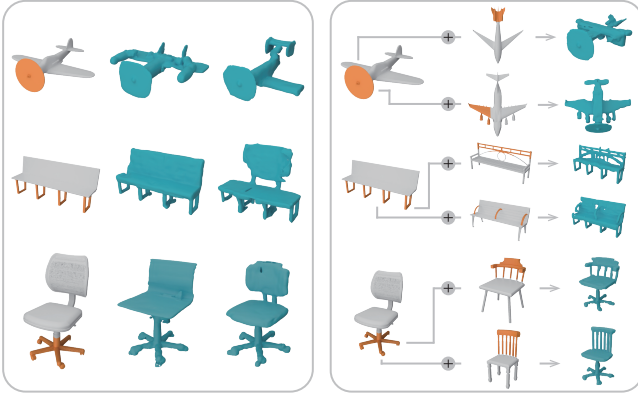


Fig. 7. Part-conditioned shape completion and blending enabled by our patch-based MASH representation.

Limitation and future work. As a preliminary attempt, our representation and corresponding optimization still have several limitations. Our current MASH representation only considers geometry and it would be interesting to explore ways to further incorporate textures. For the optimization, the current initialization evenly distributes anchors over the given data, which sometimes lead to sub-optimal fitting results. Adapting the anchor distribution to the given shape will be a promising direction for future work. Additionally, our current optimization strategy is relatively sensitive to outliers, which are commonly presented in range sensor scans and can cause reconstruction artifacts. Enhancing the robustness and efficiency of optimization warrants further in-depth investigation.

REFERENCES

- Nina Amenta, Marshall Bern, and Manolis Kamvysselis. 1998. A new Voronoi-based surface reconstruction algorithm. In *Proceedings of the 25th Annual Conference on Computer Graphics and Interactive Techniques (SIGGRAPH '98)*. Association for Computing Machinery, New York, NY, USA, 415–421. <https://doi.org/10.1145/280814.280947>
- Nina Amenta, Sunghee Choi, and Ravi Krishna Kolluri. 2001. The power crust. In *Proceedings of the Sixth ACM Symposium on Solid Modeling and Applications (Ann Arbor, Michigan, USA) (SMA '01)*. Association for Computing Machinery, New York, NY, USA, 249–266. <https://doi.org/10.1145/376957.376986>
- F. Bernardini, J. Mittleman, H. Rushmeier, C. Silva, and G. Taubin. 1999. The ball-pivoting algorithm for surface reconstruction. *IEEE Transactions on Visualization and Computer Graphics* 5, 4 (1999), 349–359. <https://doi.org/10.1109/2945.817351>
- Andrew Brock, Theodore Lim, James M Ritchie, and Nick Weston. 2016. Generative and discriminative voxel modeling with convolutional neural networks. *arXiv preprint arXiv:1608.04236* (2016).
- Fatih Calakli and Gabriel Taubin. 2012. *SSD-C: Smooth Signed Distance Colored Surface Reconstruction*. Springer London, London, 323–338. https://doi.org/10.1007/978-1-4471-2804-5_18
- Angel X. Chang, Thomas A. Funkhouser, Leonidas J. Guibas, Pat Hanrahan, Qi-Xing Huang, Zimo Li, Silvio Savarese, Manolis Savva, Shuran Song, Hao Su, Jianxiong Xiao, Li Yi, and Fisher Yu. 2015. ShapeNet: An Information-Rich 3D Model Repository. *CoRR abs/1512.03012* (2015). arXiv:1512.03012 <http://arxiv.org/abs/1512.03012>
- Yen-Chi Cheng, Hsin-Ying Lee, Sergey Tulyakov, Alexander G Schwing, and Liang-Yan Gui. 2023. Sdfusion: Multimodal 3d shape completion, reconstruction, and generation. In *Proceedings of the IEEE/CVF Conference on Computer Vision and Pattern Recognition*. 4456–4465.
- Christopher B Choy, Danfei Xu, JunYoung Gwak, Kevin Chen, and Silvio Savarese. 2016. 3d-r2n2: A unified approach for single and multi-view 3d object reconstruction. In *Computer Vision–ECCV 2016: 14th European Conference, Amsterdam, The Netherlands, October 11–14, 2016, Proceedings, Part VIII* 14. Springer, 628–644.
- Angela Dai, Charles Ruizhongtai Qi, and Matthias Nießner. 2017. Shape completion using 3d-encoder-predictor cnns and shape synthesis. In *Proceedings of the IEEE conference on computer vision and pattern recognition*. 5868–5877.
- Matt Deitke, Dustin Schwenk, Jordi Salvador, Luca Weihs, Oscar Michel, Eli VanderBilt, Ludwig Schmidt, Kiana Ehsani, Aniruddha Kembhavi, and Ali Farhadi. 2023. Obaverse: A universe of annotated 3d objects. In *Proceedings of the IEEE/CVF Conference on Computer Vision and Pattern Recognition*. 13142–13153.
- Tamal K. Dey and Samrat Goswami. 2004. Provable surface reconstruction from noisy samples. In *Proceedings of the Twentieth Annual Symposium on Computational Geometry (Brooklyn, New York, USA) (SCG '04)*. Association for Computing Machinery, New York, NY, USA, 330–339. <https://doi.org/10.1145/997817.997867>
- Herbert Edelsbrunner and Ernst P. Mücke. 1994. Three-dimensional alpha shapes. *ACM Trans. Graph.* 13, 1 (jan 1994), 43–72. <https://doi.org/10.1145/174462.156635>
- Rohit Girdhar, David F Fouhey, Mikel Rodriguez, and Abhinav Gupta. 2016. Learning a predictable and generative vector representation for objects. In *Computer Vision–ECCV 2016: 14th European Conference, Amsterdam, The Netherlands, October 11–14, 2016, Proceedings, Part VI* 14. Springer, 484–499.
- Shunwang Gong, Lei Chen, Michael Bronstein, and Stefanos Zafeiriou. 2019. SpiralNet++: A Fast and Highly Efficient Mesh Convolution Operator. *arXiv:1911.05856 [cs.CV]*
- William J Gordon and Richard F Riesenfeld. 1974. B-spline curves and surfaces. In *Computer aided geometric design*. Elsevier, 95–126.
- Anchit Gupta, Wenhan Xiong, Yixin Nie, Ian Jones, and Barlas Oğuz. 2023. 3dgen: Triplane latent diffusion for textured mesh generation. *arXiv preprint arXiv:2303.05371* (2023).
- Rana Hanocka, Amir Hertz, Noa Fish, Raja Giryes, Shachar Fleishman, and Daniel Cohen-Or. 2019. MeshCNN: a network with an edge. *ACM Transactions on Graphics* 38, 4 (July 2019), 1–12. <https://doi.org/10.1145/3306346.3322959>
- Hugues Hoppe, Tony DeRose, Tom Duchamp, John McDonald, and Werner Stuetzle. 1992. Surface reconstruction from unorganized points. *SIGGRAPH Comput. Graph.* 26, 2 (jul 1992), 71–78. <https://doi.org/10.1145/142920.134011>
- Ka-Hei Hui, Aditya Sanghi, Arianna Rampini, Kamal Rahimi Malekshan, Zhengze Liu, Hooman Shayani, and Chi-Wing Fu. 2024. Make-a-shape: a ten-million-scale 3d shape model. In *Forty-first International Conference on Machine Learning*.
- Andrés Iglesias, G Echevarría, and Akemi Gálvez. 2004. Functional networks for B-spline surface reconstruction. *Future Generation Computer Systems* 20, 8 (2004), 1337–1353.
- Heewoo Jun and Alex Nichol. 2023. Shap-e: Generating conditional 3d implicit functions. *arXiv preprint arXiv:2305.02463* (2023).
- Sagi Katz and Ayallet Tal. 2015. On the visibility of point clouds. In *Proceedings of the IEEE international conference on computer vision*. 1350–1358.
- Michael Kazhdan, Matthew Bolitho, and Hugues Hoppe. 2006. Poisson surface reconstruction. In *Proceedings of the Fourth Eurographics Symposium on Geometry Processing (<conf-loc>, <city>Cagliari</city>, <state>Sardinia</state>, <country>Italy</country>, </conf-loc>) (SGP '06)*. Eurographics Association, Goslar, DEU, 61–70.
- Michael Kazhdan and Hugues Hoppe. 2013. Screened poisson surface reconstruction. *ACM Transactions on Graphics (ToG)* 32, 3 (2013), 1–13.
- Benjamin Keiner, Matthias Innmann, Michael Sänger, and Marc Stamminger. 2015. Spherical fibonacci mapping. *ACM Transactions on Graphics (TOG)* 34, 6 (2015), 1–7.
- Bernhard Kerbl, Georgios Kopanas, Thomas Leimkühler, and George Drettakis. 2023. 3D Gaussian splatting for real-time radiance field rendering. *ACM Trans. Graph.* 42, 4 (2023), 139–1.
- Yushi Lan, Fangzhou Hong, Shuai Yang, Shangchen Zhou, Xuyi Meng, Bo Dai, Xinggang Pan, and Chen Change Loy. 2025. Ln3diff: Scalable latent neural fields diffusion for speedy 3d generation. In *European Conference on Computer Vision*. Springer, 112–130.
- Sixu Li, Chaojian Li, Wenbo Zhu, Boyang Yu, Yang Zhao, Cheng Wan, Haoran You, Huihong Shi, and Yingyan Lin. 2023. Instant-3d: Instant neural radiance field training towards on-device ar/vr 3d reconstruction. In *Proceedings of the 50th Annual International Symposium on Computer Architecture*. 1–13.
- Isaak Lim, Alexander Dielen, Marcel Campen, and Leif Kobbelt. 2018. A Simple Approach to Intrinsic Correspondence Learning on Unstructured 3D Meshes. *arXiv:1809.06664 [cs.CV]*
- Siyou Lin, Dong Xiao, Zuoqiang Shi, and Bin Wang. 2022. Surface Reconstruction from Point Clouds without Normals by Parametrizing the Gauss Formula. *ACM Trans. Graph.* 42, 2, Article 14 (oct 2022), 19 pages. <https://doi.org/10.1145/3554730>
- Ruoshi Liu, Rundi Wu, Basile Van Hoorick, Pavel Tokmakov, Sergey Zakharov, and Carl Vondrick. 2023. Zero-1-to-3: Zero-shot one image to 3d object. In *Proceedings of the IEEE/CVF international conference on computer vision*. 9298–9309.
- William E. Lorensen and Harvey E. Cline. 1987. Marching cubes: A high resolution 3D surface construction algorithm. *SIGGRAPH Comput. Graph.* 21, 4 (aug 1987), 163–169. <https://doi.org/10.1145/37402.37422>
- Lars Mescheder, Michael Oechsle, Michael Niemeyer, Sebastian Nowozin, and Andreas Geiger. 2019. Occupancy networks: Learning 3d reconstruction in function space. In *Proceedings of the IEEE/CVF conference on computer vision and pattern recognition*. 4460–4470.
- Gal Metzger, Rana Hanocka, Denis Zorin, Raja Giryes, Daniele Panozzo, and Daniel Cohen-Or. 2021. Orienting Point Clouds with Dipole Propagation. *ACM Trans.*

- Graph.* 40, 4 (2021).
- Ben Mildenhall, Pratul P Srinivasan, Matthew Tancik, Jonathan T Barron, Ravi Ramamoorthi, and Ren Ng. 2021. Nerf: Representing scenes as neural radiance fields for view synthesis. *Commun. ACM* 65, 1 (2021), 99–106.
- Charlie Nash, Yaroslav Ganin, SM Ali Eslami, and Peter Battaglia. 2020. Polygen: An autoregressive generative model of 3d meshes. In *International conference on machine learning*. PMLR, 7220–7229.
- Alex Nichol, Heewoo Jun, Prafulla Dhariwal, Pamela Mishkin, and Mark Chen. 2022. Point-e: A system for generating 3d point clouds from complex prompts. *arXiv preprint arXiv:2212.08751* (2022).
- Maxime Oquab, Timothée Darret, Théo Moutakanni, Huy Vo, Marc Szafraniec, Vasil Khalidov, Pierre Fernandez, Daniel Haziza, Francisco Massa, Alaeldin El-Nouby, et al. 2023. Dinov2: Learning robust visual features without supervision. *arXiv preprint arXiv:2304.07193* (2023).
- Jeong Joon Park, Peter Florence, Julian Straub, Richard Newcombe, and Steven Lovegrove. 2019. DeepSDF: Learning Continuous Signed Distance Functions for Shape Representation. *arXiv:1901.05103 [cs.CV]*
- Songyu Peng, Michael Niemeyer, Lars Mescheder, Marc Pollefeys, and Andreas Geiger. 2020. Convolutional Occupancy Networks. In *Computer Vision – ECCV 2020*, Andrea Vedaldi, Horst Bischof, Thomas Brox, and Jan-Michael Frahm (Eds.). Springer International Publishing, Cham, 523–540.
- Xavier Pennec. 1998. *Computing the mean of geometric features application to the mean rotation*. Ph.D. Dissertation. INRIA.
- Ben Poole, Ajay Jain, Jonathan T Barron, and Ben Mildenhall. 2022. Dreamfusion: Text-to-3d using 2d diffusion. *arXiv preprint arXiv:2209.14988* (2022).
- Marie-Julie Rakotosaona, Paul Guerrero, Noam Aigerman, Niloy Mitra, and Maks Ovsjanikov. 2021. Learning Delaunay Surface Elements for Mesh Reconstruction. In *2021 IEEE/CVF Conference on Computer Vision and Pattern Recognition (CVPR)*. 22–31. <https://doi.org/10.1109/CVPR46437.2021.00009>
- Ravi Ramamoorthi. 2023. Nerfs: The search for the best 3d representation. *arXiv preprint arXiv:2308.02751* (2023).
- Aditya Ramesh, Mikhail Pavlov, Gabriel Goh, Scott Gray, Chelsea Voss, Alec Radford, Mark Chen, and Ilya Sutskever. 2021. Zero-shot text-to-image generation. In *International conference on machine learning*. PMLR, 8821–8831.
- Robin Rombach, Andreas Blattmann, Dominik Lorenz, Patrick Esser, and Björn Ommer. 2022. High-resolution image synthesis with latent diffusion models. In *Proceedings of the IEEE/CVF conference on computer vision and pattern recognition*. 10684–10695.
- Chitwan Saharia, William Chan, Saurabh Saxena, Lala Li, Jay Whang, Emily L Denton, Kamyar Ghasemipour, Raphael Gontijo Lopes, Burcu Karagol Ayan, Tim Salimans, et al. 2022. Photorealistic text-to-image diffusion models with deep language understanding. *Advances in neural information processing systems* 35 (2022), 36479–36494.
- Dietmar Saupe and Dejan Vranić. 2001. 3D model retrieval with spherical harmonics and moments. In *Joint Pattern Recognition Symposium*. Springer, 392–397.
- Shy Shalom, Ariel Shamir, Hao Zhang, and Daniel Cohen-Or. 2010. Cone Carving for Surface Reconstruction. *ACM Transactions on Graphics, Proceedings Siggraph Asia* 29, 5 (2010).
- Lior Shapira, Ariel Shamir, and Daniel Cohen-Or. 2008. Consistent mesh partitioning and skeletonisation using the shape diameter function. *The Visual Computer* 24, 4 (2008), 249–259.
- Yawar Siddiqui, Antonio Alliegro, Alexey Artemov, Tatiana Tommasi, Daniele Sirigatti, Vladislav Rosov, Angela Dai, and Matthias Nießner. 2024. Meshgpt: Generating triangle meshes with decoder-only transformers. In *Proceedings of the IEEE/CVF Conference on Computer Vision and Pattern Recognition*. 19615–19625.
- Yizhi Wang, Zeyu Huang, Ariel Shamir, Hui Huang, Hao Zhang, and Ruizhen Hu. 2023. ARO-Net: Learning Implicit Fields from Anchored Radial Observations. *CVPR* (2023).
- Jiajun Wu, Chengkai Zhang, Tianfan Xue, Bill Freeman, and Josh Tenenbaum. 2016. Learning a probabilistic latent space of object shapes via 3d generative-adversarial modeling. *Advances in neural information processing systems* 29 (2016).
- Zhirong Wu, Shuran Song, Aditya Khosla, Fisher Yu, Linguang Zhang, Xiaou Tang, and Jianxiong Xiao. 2015. 3d shapenets: A deep representation for volumetric shapes. In *Proceedings of the IEEE conference on computer vision and pattern recognition*. 1912–1920.
- Yiheng Xie, Towaki Takikawa, Shunsuke Saito, Or Litany, Shiqin Yan, Numair Khan, Federico Tombari, James Tompkin, Vincent Sitzmann, and Srinath Sridhar. 2022. Neural Fields in Visual Computing and Beyond. (2022).
- Jiale Xu, Weihao Cheng, Yiming Gao, Xintao Wang, Shenghua Gao, and Ying Shan. 2024. Instantmesh: Efficient 3d mesh generation from a single image with sparse-view large reconstruction models. *arXiv preprint arXiv:2404.07191* (2024).
- Xianghui Yang, Huiwen Shi, Bowen Zhang, Fan Yang, Jiaceng Wang, Hongxu Zhao, Xinhai Liu, Xinzhou Wang, Qingxiang Lin, Jiaao Yu, et al. 2024. Hunyuan3d-1.0: A unified framework for text-to-3d and image-to-3d generation. *arXiv preprint arXiv:2411.02293* (2024).
- Biao Zhang, Jiapeng Tang, Matthias Niessner, and Peter Wonka. 2023. 3dshape2vecset: A 3d shape representation for neural fields and generative diffusion models. *ACM Transactions on Graphics (TOG)* 42, 4 (2023), 1–16.
- Longwen Zhang, Ziyu Wang, Qixuan Zhang, Qiwei Qiu, Anqi Pang, Haoran Jiang, Wei Yang, Lan Xu, and Jingyi Yu. 2024. CLAY: A Controllable Large-scale Generative Model for Creating High-quality 3D Assets. *ACM Transactions on Graphics (TOG)* 43, 4 (2024), 1–20.
- Xi Zhao, Ruizhen Hu, Paul Guerrero, Niloy Mitra, and Taku Komura. 2016. Relationship templates for creating scene variations. *ACM Transactions on Graphics* 35, 6 (2016), 1–13.
- Zibo Zhao, Wen Liu, Xin Chen, Xianfang Zeng, Rui Wang, Pei Cheng, Bin Fu, Tao Chen, Gang Yu, and Shenghua Gao. 2024. Michelangelo: Conditional 3d shape generation based on shape-image-text aligned latent representation. *Advances in Neural Information Processing Systems* 36 (2024).

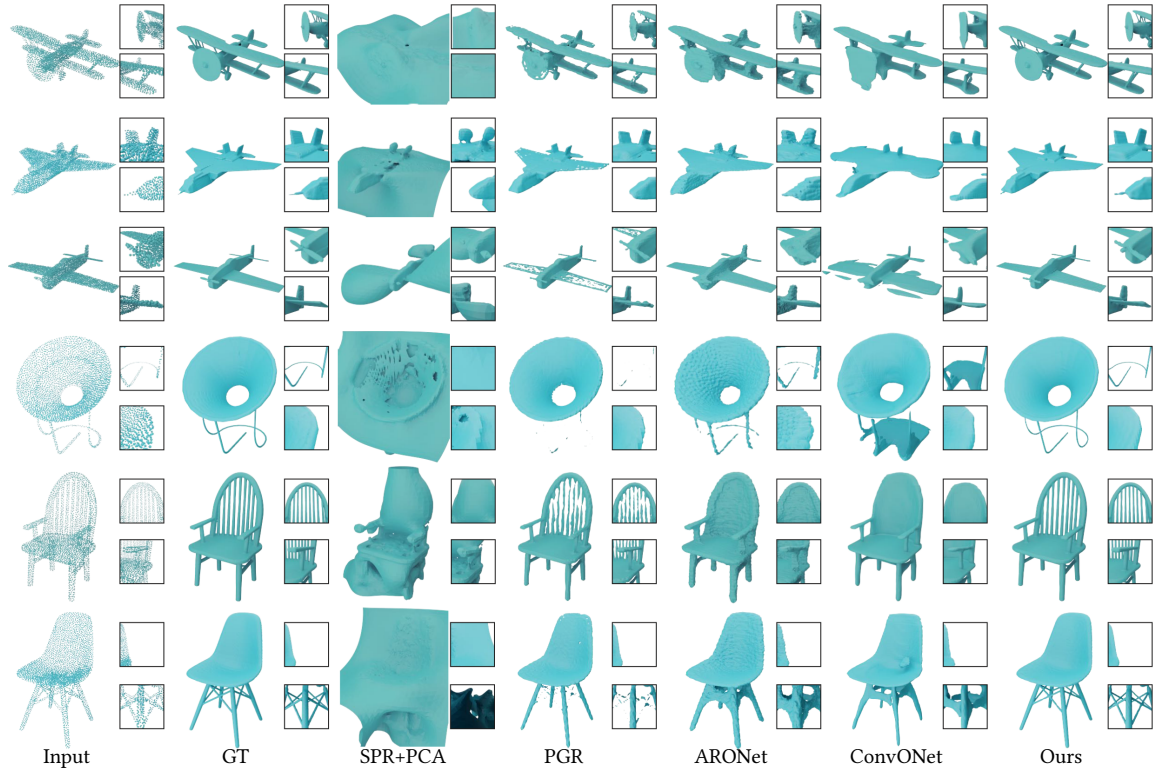


Fig. 8. Qualitative results on surface reconstruction with different methods. We additionally select two details for each result to show the performance of all methods better.

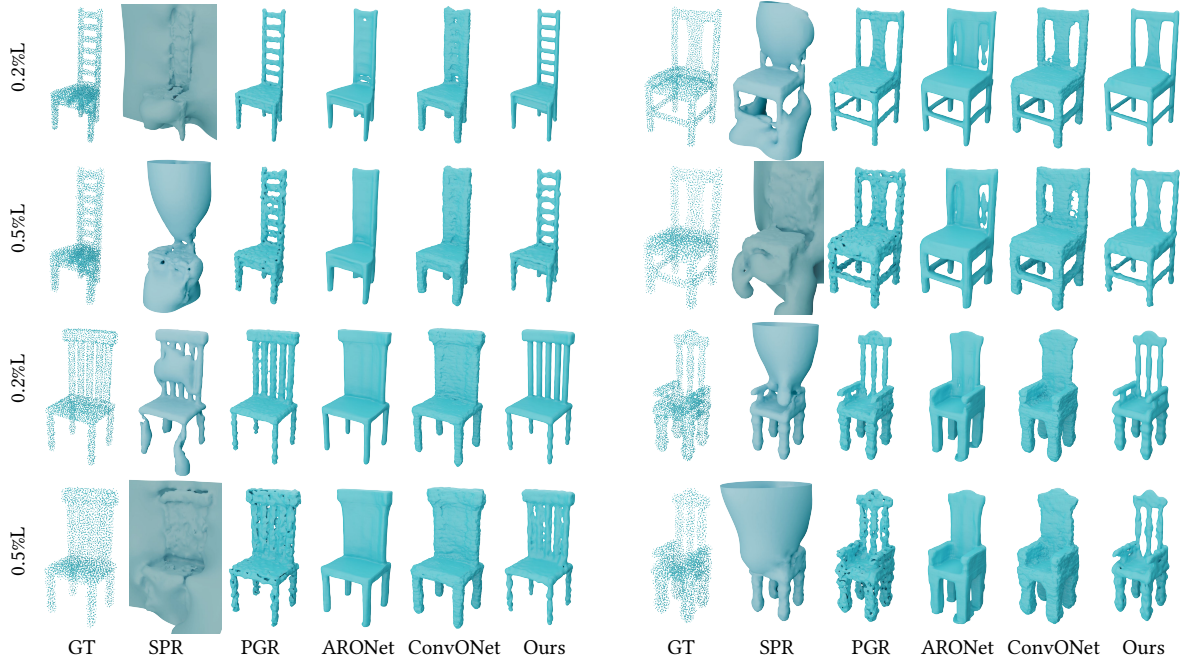


Fig. 9. Reconstructions on the chair category with two different noise levels.

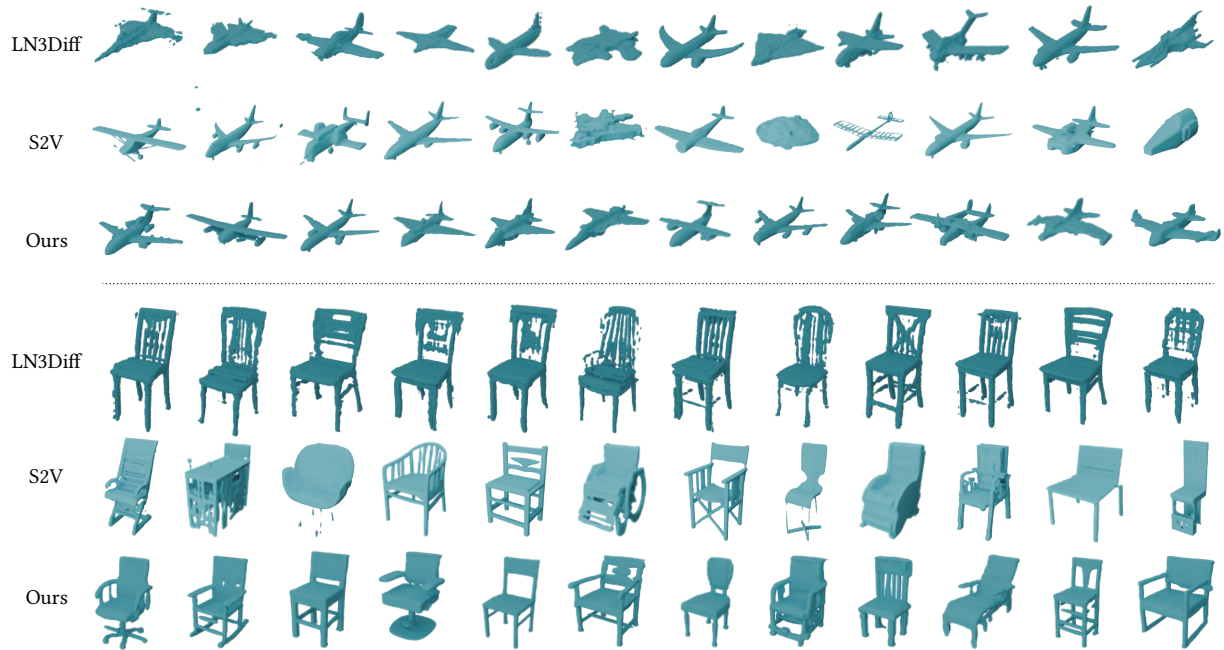


Fig. 10. Qualitative results on category-conditioned generation compared with different methods.

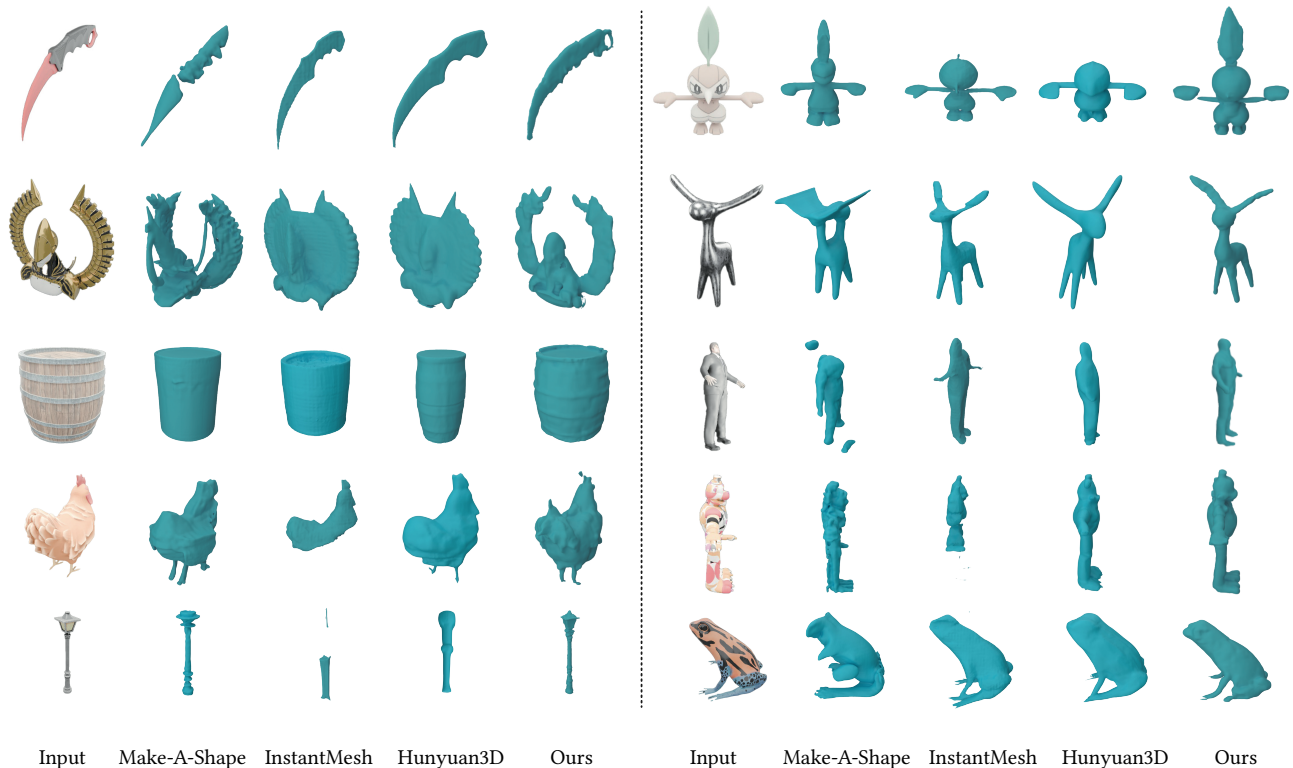


Fig. 11. Qualitative results on single image to 3D generation compared with different methods.